Geochemistry, Geophysics, Geosystems®

AGU ADVANCING EARTH AND SPACE SCIENCES

RESEARCH ARTICLE
10.1029/2023GC011242

Asymmetric Dipole Trends in Geodynamo Models and the Paleomagnetic Field

B. A. Buffett[1]

[1]Department of Earth and Planetary Science, University of California, Berkeley, Berkeley, CA, USA

Key Points:

- Skewed dipole trends are predicted in geodynamo models under a restricted set of boundary conditions
- Skewness in the models is correlated with fluid upwelling and magnetic-flux expulsion at the core-mantle boundary
- Trends in the paleomagnetic field imply large flux-expulsion events on millennial timescales

Correspondence to:
B. A. Buffett,
bbuffett@berkeley.edu

Citation:
Buffett, B. A. (2023). Asymmetric dipole trends in geodynamo models and the paleomagnetic field. *Geochemistry, Geophysics, Geosystems*, *24*, e2023GC011242. https://doi.org/10.1029/2023GC011242

Received 15 SEP 2023
Accepted 28 NOV 2023

Abstract Temporal trends in the paleomagnetic dipole moment exhibit the property of positive skewness. On average, positive trends are larger and occur less frequently than negative trends over timescales of several tens of kyr. We explore the origin of this property using numerical geodynamo models. A suite of models reveals that skewness arises for a restricted set of boundary conditions. Models driven by heat flow at the top and bottom boundaries exhibit very little skewness, whereas models driven solely by heat flow on the lower boundary produce significant positive skewness. Further increases in skewness occur in the presence of thermal stratification at the top of the core. The level of skewness in the geodynamo models is correlated with estimates of upwelling near the core-mantle boundary. Sustained upwelling is expected to increase magnetic-flux expulsion, contributing to higher levels of skewness. Similar behavior is recovered from stochastic models in which the dipole is generated by a random series of cyclonic convection events. Skewness in the stochastic models is quantitatively similar to estimates from the geodynamo models when the average recurrence time of the convection events is 100 years. Extending the stochastic models to the paleomagnetic field implies a longer recurrence time of 1,000 years or more. We interpret this recurrence time in terms of the timing of flux-expulsion events rather than individual convective events. Abrupt increases in the dipole moment from flux expulsion can produce skewed trends on timescales of tens of kyr.

Plain Language Summary Paleomagnetic observations suggest that the dipole field grows and decays at different rates. Abrupt growth of the dipole is often followed by slower decay, particularly when averaged over short-period fluctuations. Geodynamo models are capable of reproducing this behavior, but only with a restricted set of the boundary conditions. Many features of the geodynamo models are captured in stochastic models when the dipole generation is represented as a series of cyclonic convection events. The average recurrence time for the cyclonic convection events is the main factor in setting the level of asymmetry. Extending these results to the paleomagnetic field implies a recurrence time of several kyr. Such long recurrence times cannot be attributed to individual convection events when the timescale for fluid to rise through the core is only 100 years. Instead, we attribute the long recurrences times to magnetic-flux expulsion. Large flux-expulsion events occurring on kyr timescales are sufficient to account for the observed asymmetry.

1. Introduction

Trends in the paleomagnetic dipole moment contain a wealth of information about the generation of Earth's magnetic field. Quantitative insights are recovered from a statistical assessment of the trends. Time series can be analyzed for the mean, variance and higher-order moments. Of particular interest is the third-order moment for skewness because it reflects asymmetries in the growth and decay of the dipole. The study of Ziegler and Constable (2011) was the first to report evidence for asymmetry during times of stable polarity. They analyzed the paleomagnetic model PADM2M (Ziegler et al., 2011) and found the dipole spent less time growing than decaying over the past 2 Myr. This observation was supported by Avery et al. (2017) using skewness as a measure of the asymmetry. Positive skewness was reported for PADM2M, implying that positive trends were larger and less frequent than negative trends. This behavior is evident in the PADM2M time series on timescales of a few 10s of kyr (see Figure 1a). Additional support for positive skewness was found by Avery et al. (2017) in a high-resolution record of seafloor magnetization with ages between 9.3 and 11.2 Ma.

A separate source of information comes from the variance of dipole trends, particularly when the duration of the trend is varied (Buffett et al., 2019). Results from several paleomagnetic models reveal systematic changes in the computed trends. Different durations are sampled using 2-Myr records from the SINT-2000 (Valet et al., 2005) and PADM2M (Ziegler et al., 2011) models, an intermediate resolution 100-kyr model (Panovska et al., 2018),

10.1029/2023GC011242

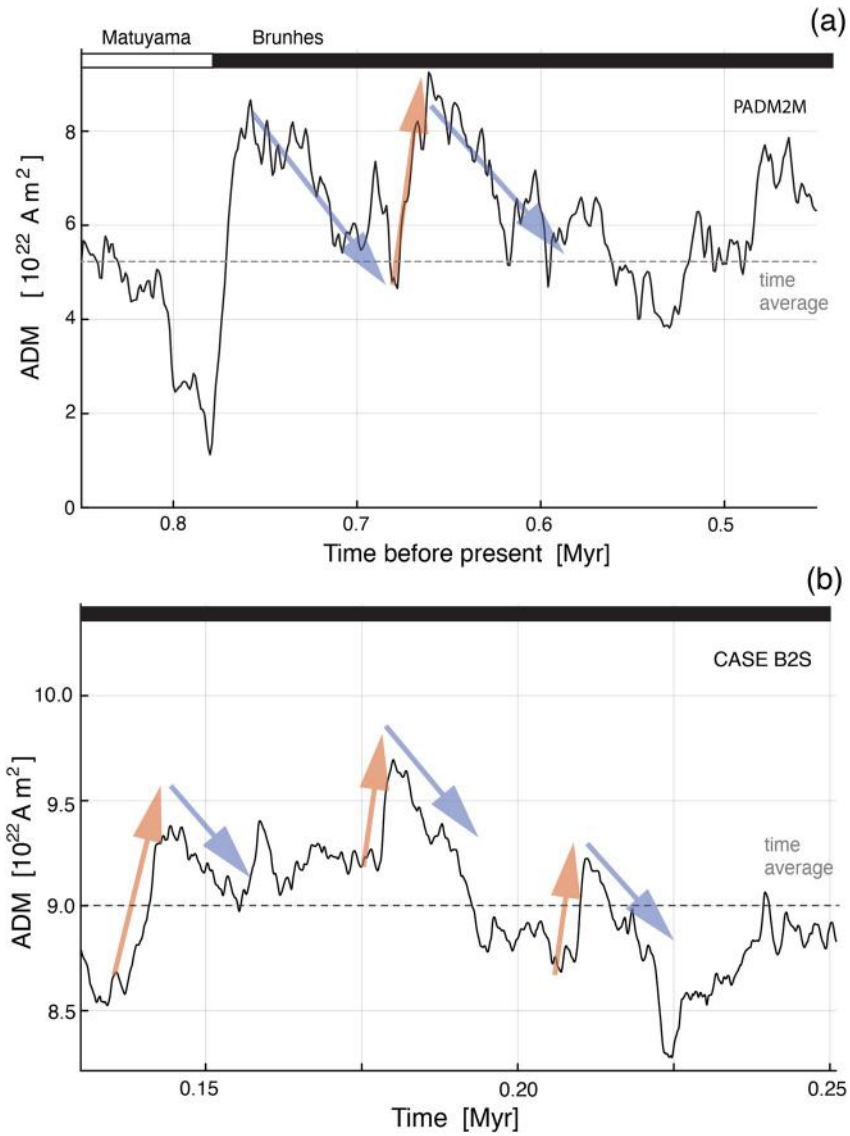

Figure 1. Time dependence of the axial dipole moment (ADM) from the PADM2M model (a) and a geodynamo model (b). Trends in the paleomagnetic record are asymmetric on timescales of a few 10s of kyr, whereas the geodynamo models have asymmetric trends on shorter timescales (typically less than 5 kyr). In both cases abrupt increases in ADM (red) are often followed by slower decreases (blue) when averaged over short-period fluctuations.

and a high-resolution 10-kyr model (Constable et al., 2016). The full range of variability in these paleomagnetic records is reproduced by a simple stochastic model (e.g., Nijsse et al., 2019). The question we address here is whether the variance and skewness of dipole trends in the paleomagnetic record can be reproduced in geodynamo models. Success in reproducing these statistics with geodynamo models means that we can probe the numerical results to uncover the origin of this behavior and assess the implications for the paleomagnetic record.

We begin in Section 2 by describing the geodynamo models used in this study. We extend the study of Avery et al. (2019) by adopting boundary conditions that promote different styles of convection. Dipole trends from the geodynamo models are presented in Section 3. All models give qualitatively similar results for the variance of the trends, but the skewness is sensitive to the choice of boundary conditions. No skewness is obtained in models when convection is driven by heat flow at the top and bottom boundaries. By comparison positive skewness emerges when convection is driven solely by heat flow at the bottom boundary. One example of skewed trends from the geodynamo models is shown in Figure 1b. Here the timescale for the skewed trends is shorter than that for the paleomagnetic record (typically less than 5 kyr compared with several tens of kyr).

Table 1
Summary of Geodynamo Models

Case	*Ra*	*Qt*	*Pm*	$T(r_i)$	$T(r_o)$	*dT/dr*	u_{rms}	B_{rms}	$t_{\max}$
TB0	1,000	0	1.0	1.0	−0.13	−1.8	135.5	2.45	3.13
TB1	1,200	0	1.0	1.0	−0.19	−2.2	164.9	2.57	2.78
B2	1,100	−3.66	1.0	1.0	0.03	0.0	129.2	1.72	8.52
B3	1,300	−4.32	1.0	1.0	0.01	0.0	150.2	1.85	4.06
B3Pm	1,550	−5.30	0.8	1.0	−0.02	0.0	184.0	1.64	4.07
B2S	1,100	−5.10	1.0	1.0	0.0	0.44	130.8	1.60	3.51

Note. All models are computed using Ekman number $Ek = 5 \times 10^{-5}$ and Prandtl number Pr = 1. *Ra* is the modified Rayleigh number, *Qt* is the dimensionless heat sink, *Pm* is the magnetic Prandtl number, $T(r_i)$ and $T(r_o)$ are the fixed or computed average temperatures at the ICB and CMB, *dT/dr* is the radial temperature gradient at the CMB, u_{rms} is the volume averaged, root-mean-square (rms) velocity, B_{rms} is the corresponding rms magnetic field and $t_{\max}$ is the duration of the calculation in viscous diffusion times.

Analysis of the geodynamo models in Section 4 suggest that skewness originates from processes near the top boundary. A quantitative assessment of magnetic-flux expulsion accounts for the differences between the models. Larger and less frequent flux expulsion events are associated with higher levels of skewness. Similar predictions are made in Section 5 using a stochastic model in which the dipole is generated by a series of random cyclonic events. Applying this model to the paleomagnetic field in Section 6 gives a timescale of 10^3 years for the recurrence of large flux-expulsion events.

2. Geodynamo Models

Six geodynamo models are used to explore the origin of skewed trends. Four of these models have previously been described in the study of Davis and Buffett (2022). Cases TB0 and TB1 are driven by heat fluxes at the top and bottom boundaries. A uniform heat flux is maintained on the top boundary and the lower boundary is held at a fixed temperature. Cases B2 and B3 are driven solely by a heat flux at the bottom boundary. Convection is sustained by combining a volumetric heat sink *Qt* with an insulating thermal condition on the top boundary. We add Cases B2S and B3Pm to expand the styles of convection under consideration. Case B2S uses a heat sink and fixed temperature conditions to promote thermal stratification when the value of *Qt* is sufficiently large. Case B3Pm is a variation on B3 to explore the dependence on magnetic Prandtl number (see below).

Numerical solutions for the velocity, **u**, magnetic, **B**, and temperature, *T*, fields are computed using the *Calypso* 1.2 code (Matsui et al., 2014, 2017). We express the solutions in non-dimensional form using the thickness *L* of the fluid shell as a length scale and the viscous diffusion time L^2/ν as the timescale, where ν is the kinematic viscosity. Velocity is scaled by ν/L and temperature is scaled the temperature difference ΔT across the fluid shell; the magnetic field is scaled by $\sqrt{\rho\mu\eta\Omega}$, where ρ is the fluid density, μ is the permeability of free space, η is the magnetic diffusivity, and Ω is the constant rotation rate of the spherical shell. Each solution is defined by five dimensionless control parameters. The vigor of convection is specified by the modified Rayleigh number

$$Ra = \frac{\alpha g \Delta T L}{\nu \Omega} \tag{1}$$

where α is the coefficient of thermal expansion and g is the acceleration due to gravity at the core-mantle boundary (CMB). The Ekman number

$$Ek = \frac{\nu}{\Omega L^2} \tag{2}$$

defines the relative importance of viscous forces. The Prandtl number

$$\mathrm{Pr} = \frac{\nu}{\kappa} \tag{3}$$

and the magnetic Prandtl number

$$Pm = \frac{\nu}{\eta} \tag{4}$$

control the influence of thermal κ and magnetic η diffusion in the solution. The final parameter is the dimensionless heat sink, *Qt*, which is used to set the style of convection (Kutzner & Christensen, 2002). We let $Qt = 0$ for cases TB0 and TB1 and adjust the value of *Qt* for cases B2, B3, and B3Pm to achieve a dimensionless temperature close to zero at the CMB (see Table 1). Case B2S fixes the temperature at the top and bottom boundaries, so the choice of *Qt* defines the magnitude and sign of the temperature gradient at the outer boundary. A positive radial temperature gradient corresponds to fluid stratification at the CMB.

Table 1 gives a summary of the input parameters and several diagnostics. All solutions are computed using $Ek = 5 \times 10^{-5}$ and Pr = 1. We vary the value of *Ra* for Cases TB0 and TB1, and for Cases B2 and B3 to adjust

the vigor of convection in these two configurations. Five of the six cases use $Pm = 1$. The exception is Case B3Pm, which uses a lower value of $Pm = 0.8$ and a higher value of Ra. The goal is to maintain a broadly consistent value for the magnetic Reynolds number with the different choices of Pm. We also include in Table 1 the volume-averaged, root-mean-square (rms) velocity, u_{rms}, and magnetic field, B_{rms}. These values are taken to represent typical velocities, U, and magnetic fields, B, in the solutions. With our choice of scales the value of u_{rms} gives an estimate for the Reynolds number

$$\mathrm{Re} = \frac{UL}{\nu}, \tag{5}$$

whereas the magnetic Reynolds number is

$$Rm = \frac{UL}{\eta} = Pm\,\mathrm{Re}. \tag{6}$$

The nondimensional value of B_{rms}^2 corresponds to the Elsasser number

$$\Lambda = \frac{\sigma B^2}{\rho\Omega}, \tag{7}$$

which is often used to quantify the relative importance of the magnetic force to the Coriolis force (Aurnou & King, 2017). Here $\sigma = 1/\mu\eta$ is the electrical conductivity of the fluid.

Solutions are converted to dimensional form using a representative value for the magnetic diffusivity $\eta = 0.8$ m^2 s^{-1} (Gomi & Hirose, 2015). We let $\nu = Pm\,\eta$ and $L = 2.26 \times 10^6$ m to obtain a viscous diffusion time of 202 (or 253) kyr for $Pm = 1$ (or 0.8). The corresponding dipole decay time is 48 kyr, although turbulent diffusion can shorten the effective decay time (see Section 5). The scale for the magnetic field was previously defined as $\sqrt{\rho\mu\eta\Omega}$. Setting $\rho = 10^4$ kg m^3, $\mu = 4\pi \times 10^{-7}$ H m^{-1} and $\Omega = 0.73 \times 10^{-4}$ s^{-1} gives a magnetic scale of 0.86 mT. We use this scale to convert the dimensionless Gauss coefficients from the simulation to dimensional values. The dimensional Gauss coefficient $g_1^0(a,t)$ at the surface $r = a$ is used to evaluate the axial dipole moment $x(t)$ according to

$$x(t) = \frac{4\pi}{\mu} g_1^0(a,t) a^3. \tag{8}$$

All geodynamo models produce dipolar and non-reversing fields. The time-averaged axial dipole moment (and standard deviation) vary between $7.96 \pm 0.33 \times 10^{22}$ A m^2 for Case B2 and $13.09 \pm 0.751 \times 10^{22}$ A m^2 for Case TB1.

3. Trends in the Dipole Moment

Time series $x(t)$ from the geodynamo models are used to compute trends over a prescribed time interval (denoted by w). Each solution is divided into a set of non-overlapping time intervals of length w. Trends are computed by a least-squares fit of $x(t)$ to a linear function

$$x(t) = a + bt + \epsilon, \tag{9}$$

over the chosen time interval. Here ϵ is the deviation from the linear trend. The input time series yields a set of n individual trends, b_i, depending on the value of w. We compute the variance of the trends, σ_b^2, using

$$\sigma_b^2 = \sum_{i=1}^{n} \frac{(b_i - \langle b_i \rangle)^2}{n-1} \tag{10}$$

and the skewness, s, using

$$s = \frac{\frac{1}{n}\left[\sum_{i=1}^{n} (b_i - \langle b_i \rangle)^3\right]}{\frac{1}{n}\left[\sum_{i=1}^{n} (b_i - \langle b_i \rangle)^2\right]^{3/2}} \tag{11}$$

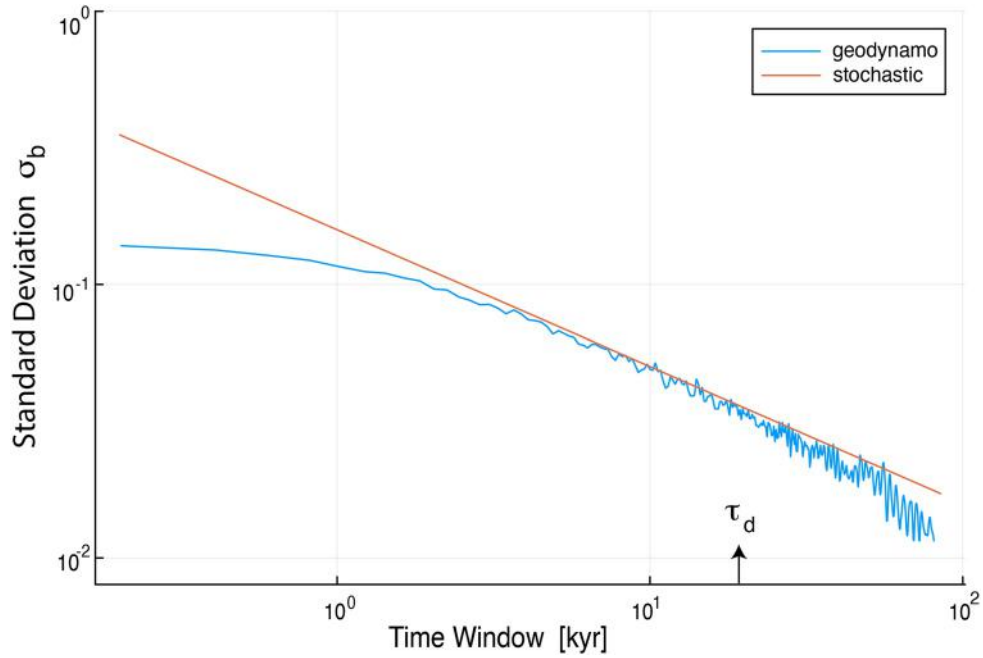

Figure 2. Standard deviation of dipole trends as a function of time window w. Trends from geodynamo model B3 are compared with the predictions of a stochastic model. Departures between the geodynamo and stochastic models at short w are due to the use of uncorrelated noise in the stochastic model. Departures are also expected when w exceeds the effective dipole decay time τ_d.

where $\langle b_i \rangle$ denotes the sample mean. Reliable statistics require long time series to lower the uncertainties. This requirement is especially true when the window length w is long because the time series is subdivided into few segments. Standard errors on s are reported as (Joanes & Gill, 1989)

$$\sigma_s \approx \sqrt{\frac{6}{n}}, \tag{12}$$

whereas the uncertainty on σ_b^2 is assessed from the scatter of estimates as the time window is varied.

3.1. Variance of Trends

The variance of trends for all geodynamo models exhibit a similar dependence on w. Figure 2 shows a representative example for Case B3. Three distinct regions are identified in the dependence of σ_b on w. At short w the standard deviation is nearly independent of w. Once w exceeds several kyr the standard deviation is approximated by

$$\sigma_b = \sqrt{\frac{2D_2}{w}} \tag{13}$$

where D_2 is the diffusion coefficient for a stochastic model (details are deferred to Section 5). Predictions for this stochastic model can be extended to larger w, but it requires a more general expression for σ_b (e.g., Nijsse et al., 2019). Steeper decreases in σ_b are expected in the stochastic model once w exceeds the effective dipole decay time (nominally 20 kyr for Case B3). These expectations are compatible with what we observe in Figure 2 for Case B3. At short w the discrepancy between the geodynamo and stochastic model is attributed to the use of uncorrelated noise in the stochastic model. Introducing correlated noise in the stochastic models reduces the fluctuations in $x(t)$ at short time intervals, which causes σ_b to saturate at small w. Previous estimates of correlated noise in geodynamo models (Buffett & Matsui, 2015; Davis & Buffett, 2022) suggest that a suitable correlation time is a fraction of the overturn time, L/U. We can reconcile the geodynamo and stochastic models if we adopt a correlation time equal to 50% of the overturn time, corresponding to 700 years for Case B3. Similar behavior is observed in a high-resolution geodynamo model of Aubert and Gillet (2021). The value of σ_b from this

10.1029/2023GC011242

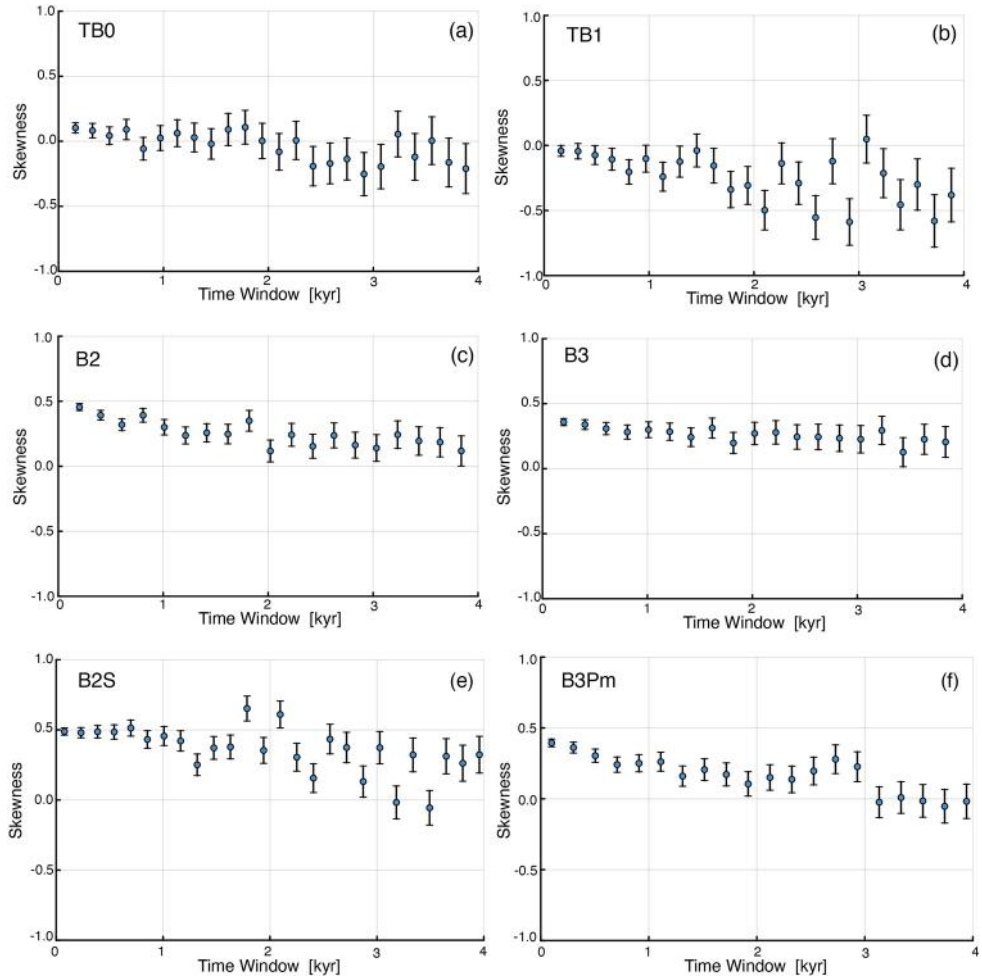

Figure 3. Skewness of trends and one-sigma uncertainty from geodynamo models as a function of time window w. (a, b) Top and bottom-driven cases TB0 and TB1 show little evidence for positive skewness. (c, d) Bottom-drive cases B2 and B3 have persistent positive skewness for all w less than 4 kyr. (e, f) Bottom-driven cases with fluid stratification (B2S) and lower Pm (B3Pm) also show persistent positive skewness.

model saturates when w drops below several hundred years rather than several thousand years. These results are expected in the high-resolution model because the overturn time is 0.12 kyr, which is about a factor of 10 shorter than the overturn time for Case B3. At larger w the standard deviation σ_b follows the $w^{-1/2}$ dependence expected from the stochastic model.

3.2. Skewness of Trends

Larger differences in skewness are reported for the geodynamo models (see Figure 3). Estimates for s in the top- and bottom-driven cases (TB0 and TB1) are generally small compared with the one-sigma uncertainties. There may be a hint of negative skewness in Case TB1, although the values rarely exceed two-sigma (One-sigma uncertainties are shown in Figure 3). By comparison, the bottom-driven cases (B2 and B3) reveal significant positive skewness. The largest skewnesses occur at the smallest w, and estimates appear to decrease slowly at larger w. While the positive skewness for Cases B2 and B3 persists over the entire range of w, the statistical significance of s is reduced at larger w because of larger uncertainties. Uncertainties in B2 and B3 are compatible with no skewness once w exceeds 4 kyr. The lower skewness and larger uncertainty at large w motivate our restriction of the window to 4 kyr.

Stratification at the top of the core increases the levels of skewness in the geodynamo models (see Figure 3e). The strength of stratification in Case B2S is quantified by the radial temperature gradient at the CMB (see Table 1).

Equivalently, we can express stratification in nondimensional form as the ratio of the buoyancy N and rotation Ω frequencies

$$\frac{N}{\Omega} = \sqrt{RaE\frac{dT}{dr}}, \tag{14}$$

where dT/dr is the nondimensional temperature gradient from Table 1. Stratification for Case B2S is $N/\Omega = 0.16$, which is weaker than the value $N/\Omega = 0.84$ proposed by Buffett et al. (2016) on the basis of magnetic-field observations. On the other hand, the layer thickness in the geodynamo model is larger than that for the proposed layer (260 vs. 140 km). The combination of layer strength and thickness in the geodynamo model produces individual estimates of s that exceed 0.5. We observe a gradual decrease in s with increasing w, although we also find larger scatter in B2S relative to B2 and B3. A longer simulation run for B2S would reduce the uncertainty in s and likely reduce the scatter at large w.

We find little direct influence of Pm on s, although the change in Pm in the geodynamo models is admittedly small. Case B3Pm has $Pm = 0.8$ and an increased Ra to maintain a nominal value of Rm. We obtain $Rm = 147$ for Case B3Pm compared with $Rm = 150$ for Case B3. The skewness for B3Pm and B3 have overlapping uncertainties, whereas a higher skewness is obtained for B2, especially at low w. The difference between B2 and B3 suggests a dependence on Rm because the higher skewness in B2 is associated with a lower value of $Rm = 129$. We explore the origin of this dependence in the next section.

4. Interpretation of Trend Statistics

Differences in the style of convection are most pronounced near the CMB. Bottom-driven convection has weaker flow in the upper part of the core, compared with the top- and bottom-driven cases. Thermal stratification causes even weaker flow near the top boundary. These differences appear to be important for the skewness of dipole trends. We explore this question by first examining the electric currents that maintain the dipole. A second, complementary perspective is offered by relating the axial dipole moment to the volume-averaged axial magnetic field in the core. Dipole generation can then be assessed in terms of aligning the axial magnetic field. When cyclonic flow produces loops of magnetic field inside the core (Parker, 1955), the upward and downward branches of the loop tend to cancel in their contribution to the average axial magnetic field. Subsequent expulsion from the core of one of the branches permits more substantial changes in the dipole (Kageyama & Sato, 1997). In this section we explore the role of the flux expulsion as a mechanism for interpreting the behavior observed in the geodynamo models.

4.1. Electric Current Fluctuations

The dipole moment $\mathbf{m}$ is defined in terms of the electric current density $\mathbf{J}$ by (e.g., Davidson, 2001)

$$\mathbf{m} = \frac{1}{2}\int_V (\mathbf{r}\times\mathbf{J})\,dV, \tag{15}$$

where $\mathbf{r}$ is the position vector and V is the volume of the core. The axial component $x = \hat{\mathbf{z}}\cdot\mathbf{m}$ is often computed using a vector spherical harmonic expansion of $\mathbf{J}$ (e.g., Chandrasekhar, 1981). Only the toroidal part of the electric current at spherical harmonic degree $l = 1$ and order $m = 0$ contributes to x, so we can write the axial dipole moment as

$$x(t) = \frac{4\pi}{3}\int_r t_{10}(r,t)r^2\,dr, \tag{16}$$

where $t_{10}(r, t)$ is the relevant toroidal coefficient of $\mathbf{J}$ at radius r and time t. (Schmidt quasi-normalization is used for spherical harmonics in *Calypso* 1.2). Snapshots of $t_{10}(r, t)$ from the geodynamo models reveal the electric current sustaining the dipole moment.

Figure 4 shows the time-averaged coefficient $t_{10}(r)$ for Cases TB1 and B3. Similar current densities occur near the bottom of the core, whereas greater differences are evident in the upper regions. Weak electric currents near $r \approx 1.4$ for Case B3 are probably a reflection of weaker local convection. Higher electric currents near the CMB

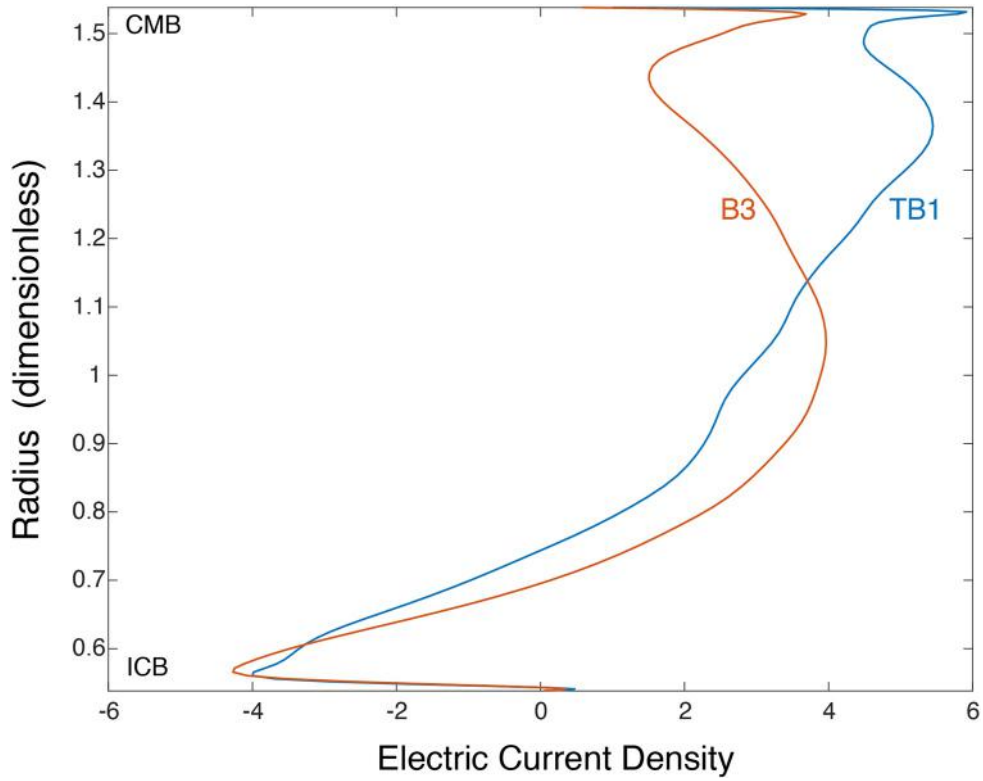

Figure 4. Toroidal electric current coefficient $t_{10}(r)$ as a function of radius r for Cases TB1 and B3. These time-averaged currents are qualitatively similar near the inner-core boundary at $r = 0.538$, but deviate more in the upper part of the core. Both profiles have a peak in electric current immediately below the CMB ($r = 1.538$). The peak value for Case TB1 is about 60% larger than that for Case B3. By comparison, the standard deviation of current fluctuations in Case TB1 is nearly 3 times larger than that for Case B3.

in Case TB1 are accompanied by much higher levels of temporal variability. To quantify this difference we report the standard deviation of temporal fluctuations at the location of the peak in $t_{10}(r)$ immediately below the CMB (see Figure 4). The standard deviation for Case TB1 is 2.8, which is nearly three times larger than the value of 1.1 for Case B3. In fact the standard deviation of $t_{10}(r)$ immediately below the CMB is a useful proxy for the level of skewness in the geodynamo trends. Part of the difference in the standard deviation is attributed to lateral flow across the CMB. Large lateral flow in Case TB1 sweeps patches of magnetic field to higher or lower latitudes, contributing to variations in the dipole moment (Livermore et al., 2020; Olson & Amit, 2006). These results suggest that the dipole trends are affected by processes near the CMB.

4.2. Magnetic Flux Expulsion

An equivalent representation for **m** from Equation 15 is possible in spherical geometries when the source of the magnetic field is confined to the volume V of the core. Using the Biot-Savart law to express **B** in terms of **J** (e.g., Jackson, 1999), the dipole moment can be written in the form

$$\mathbf{m} = \frac{3}{2\mu} \int_V \mathbf{B}\, dV. \tag{17}$$

It follows that the axial component of the dipole moment depends on the average value of B_z inside the core. Generation of B_z is usually attributed to helical flow in the core through a mechanism called the α effect (Moffatt, 1978). This type of fluid motion lifts and twists an existing magnetic field in the core to produce loops with upward and downward axial components (e.g., Parker, 1955). Cancellation between the upward and downward components is substantial, particularly when the amplitude and the length scale of the flow correspond to large Rm (Cattaneo &

Tobias, 2014). Transport and expulsion of a single limb of the loop is an effective mechanism for maintaining a strong dipolar field (Kageyama & Sato, 1997).

Flux expulsion depends on the amplitude and duration of radial flow below the CMB. The duration is an important factor in a vigorously convecting fluid because radial flow needs to be sustained long enough for diffusion to become significant. We assess the amplitude and duration of the radial flow in the geodynamo models at radius $r = 1.52$, which corresponds to a position just below the viscous boundary layer. We recover the rms radial flow as a function time for each geodynamo model and use the time average to characterize the amplitude of radial flow (denoted by u). The duration τ_u is computed from the autocorrelation function of the time series. The procedure is identical to that used to compute the effective dipole decay time from time series of $x(t)$. We integrate the autocorrelation function for the radial flow over the time lag to evaluate τ_u. The corresponding length scale l of the turbulent flow is related to u and τ_u by (e.g., Tennekes & Lumley, 1983)

$$\tau_u = \frac{l}{u}. \tag{18}$$

This relationship allows us to define a local magnetic Reynolds number $Rm^l = ul/\eta = u^2\tau_u/\eta$. Typical values for the duration of the radial flow are 20%–60% of the overturn time L/U. Values of u are also small compared with U.

How do these values relate to the efficiency of flux expulsion in the geodynamo models? Here we rely on a short-time approximation for flux expulsion, based on previous numerical models in a Cartesian geometry (Bloxham, 1986; Troyano et al., 2020). The model configuration involves a uniform initial horizontal magnetic field $B_x(0)$ in a conducting fluid, bounded above by an insulator and below by a perfect conductor. A pair of counter rotating eddies with steady velocity produce upwelling at the center of the domain and downwelling at the edges. Each eddy has size l and a constant flow amplitude u. Upwelling at the center of the domain compresses field lines toward the insulating layer. Diffusion of this magnetic field from the core produces a vertical component, B_z, in the insulating region.

Numerical solutions show that $B_z(t)$ in the insulating region increases with time until a steady state is reached (e.g., Troyano et al., 2020). Here we focus on short-time solutions at the interface with the insulating region because the duration τ_u is short compared with the time required to reach a steady state (see Appendix A for details). The short-time approximation is

$$\frac{B_z(t)}{B_x(0)} \approx C\ t^{3/2}\left(Rm^l\right)^{-1/2} \tag{19}$$

where time t is expressed in nondimensional form using the advection time $t_{adv} = l/u$ as the characteristic timescale; the constant of proportionality is $C = 5.7$ when $B_z(t)$ refers to the maximum value on the boundary at time t. Several conclusions are drawn from Equation 19. First, magnetic-flux expulsion is promoted at low Rm^l. Second, we can expect flux expulsion to increase if the flow is sustained over time. In other words, slow and sustained upwelling increases the magnitude of flux expulsion. This behavior appears to correlate with the level of skewness in the geodynamo models. Large and short-lived radial flows in TB0 and TB1 correspond to low levels of skewness. Weaker radial flow and longer durations are recovered from the bottom-driven cases, B2 and B3. Finally, the weakest flow and longest duration in Case B2S produces the highest levels of s.

Figure 5 shows the correspondence between skewness s and two attributes of the geodynamo models. One is the standard deviation of toroidal current $t_{10}(r, t)$ near the CMB. The second is the value of $B_z(t)/B_x(0)$ computed from Equation 19 at $t = \tau_u/t_{adv}$, which we take as a measure of flux expulsion in the geodynamo models. A single value of s is needed to construct this plot and we report values for each model by averaging s over windows less than $w < 1.5$ kyr. This choice partly reflects the weak dependence of s on w at short window. In addition, we expect lower uncertainties in s at short w. Increasing the range of w would lower the average because s is expected to decrease as $w^{-1/2}$ (see Section 5). However, a change in the range of w would not alter the correlations because all of the averages are changed in a similar way.

A strong correlation between s and t_{10} variance is evident in Figure 5a. Large variability in t_{10} for TB0 and TB1 corresponds to low s. Part of the variability in electric current for these cases is attributed to horizontal transport of magnetic flux over the surface of the CMB. Contributions to the dipole fluctuations from random northward and southward velocities yield trends with little skewness when the increases and decreases in $x(t)$ occur with

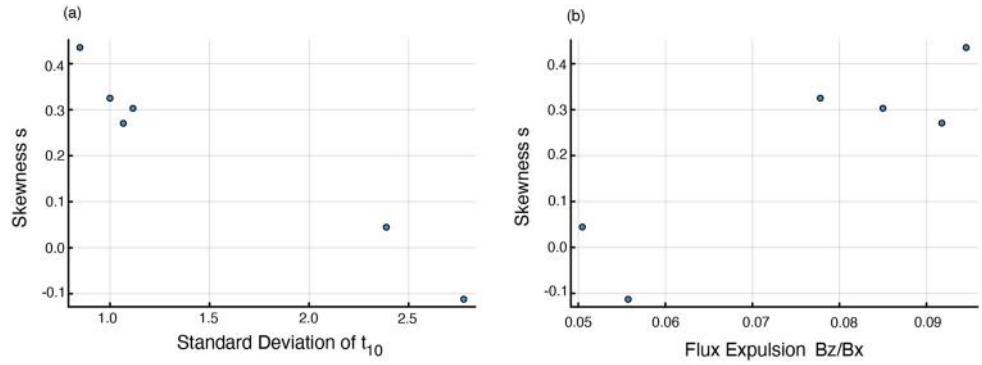

Figure 5. Correlation of trend skewness s with two attributes of the geodynamo models. (a) Change in s with the standard deviation of electric current t_{10}. (b) Change in s with the flux expulsion $B_z(t)/B_x(0)$ computed from Equation 19. High levels of skewness are correlated with low variability in the electric current and with large flux expulsion.

equal likelihood. By comparison, flux expulsion is liable to produce abrupt increases in $x(t)$, followed by periods of slower ohmic decay. Such a process should contribute to the skewness of trends. The geodynamo models show larger skewness associated with larger values of $B_z(t)/B_x(0)$. Much of the variation in $B_z(t)/B_x(0)$ is due to differences in radial flow and duration τ_u from the geodynamo models. Longer durations (or correlation times) increase $B_z(t)$, according to Equation 19. We could also reasonably expect these prolonged events to occur less often. Both of these factors are found to increase the skewness of dipole trends in the stochastic models (next section).

5. Comparison With Stochastic Models

Stochastic models are capable of reproducing many details of the trends from the geodynamo models. Because the statistics of dipole trends can be directly related to the parameters of the stochastic models, we can isolate the origin of these properties. We can also make physical connections to the geodynamo results to develop insights, which can be extended to the paleomagnetic field.

Geodynamo models fully characterize the complex interactions between the turbulent fluid motion and the magnetic field, subject to limitations in numerical resolution. These interactions sustain the magnetic field against persistent magnetic diffusion. Stochastic models for the dipole moment replace the turbulent fluid motion with a random forcing or source term $S(x, t)$. This allows us to describe the evolution of $x(t)$ in the form of a stochastic differential equation

$$\frac{dx}{dt} = S(x,t) - \frac{x}{\tau_d}, \tag{20}$$

where the random forcing $S(x, t)$ has specified statistics and the diffusive term is approximated in terms of the effective dipole decay time τ_d. One advantage of this approach is that the statistics of $S(x, t)$ can be recovered from paleomagnetic observations. Magnetic generation is expected to occur on an advective timescale, whereas dipole decay occurs on the longer τ_d timescale. These timescales differ by a factor of 20–30 in the geodynamo models, and possibly a factor of 100 in Earth's core. This separation in timescales allows us to represent S using a sequence of short (impulsive) cyclonic convection events (e.g., Levy, 1972)

$$S(x,t) = \sum_{i=0}^{N} g_i(x)\delta(t - t_i) \tag{21}$$

where $g_i(x)$ is a random amplitude and the event time t_i follows a Poisson process. While convection events are expected to have finite durations, these become minor details when focusing on the long timescale dynamics (and hence long w). On the other hand, the duration of convective events becomes important on short timescales (and hence short w). We show below that reasonable agreement with the geodynamo models requires a duration that is roughly 50% of the overturn times for the geodynamo models.

To account for the lack of skewed trends in Cases TB0 and TB1, we add a random noise term, ΔS, to the source in Equation 21. This noise term has a vanishing time average

$$< \Delta S >= 0 \tag{22}$$

and a correlation function

$$< \Delta S(t) \Delta S(t') >= q^2 \delta(t - t') \tag{23}$$

where q^2 is the variance of the white noise source. This term is intended to account for the dipole fluctuations due to random transport of magnetic field across the surface of the CMB. We expect ΔS to contribute to the variability of $x(t)$, but it cannot sustain the dipole field because the time average vanishes. Instead, generation of the dipole field is due solely to the cyclonic events. Positive and negative amplitudes are possible, but the time average must be constructive.

To complete the description of the stochastic model we need to specific the amplitudes, g_i, and the event times, t_i. The event amplitudes are defined by Scullard and Buffett (2018)

$$g_i = A_i x(t_i) f(x_i), \tag{24}$$

where A_i is a random variable that reflects the size of convective events in the core and $f(x)$ is a quenching function that suppresses field generation when the strength of the field is large. An explicit dependence on the dipole field is necessary to change the sign of g_i when the field reverses. A common form of quenching function is (e.g., Tobias, 2021)

$$f(x) = \frac{1}{1 + (x/x_0)^2}, \tag{25}$$

where x_0 is the nominal value for the onset of quenching. For simplicity, we evaluate the event times from a single Poisson process with a fixed rate parameter λ; the average recurrence time is $\theta = \lambda^{-1}$. Time increments between source events are drawn from an exponential distribution,

$$\Delta t_i = t_i - t_{i-1} \sim \mathrm{Exp}(\lambda), \tag{26}$$

and we let the convective amplitudes A_i be drawn from a uniform distribution

$$A_i \sim U(A_{\min}, A_{\max}), \tag{27}$$

where $A_{\min}$ and $A_{\max}$ are the minimum and maximum amplitudes; letting $A_{\min} < 0$ permits $S(x, t)$ to drive decreases in the dipole. However, the average amplitude must be positive to ensure that the field is sustained against ohmic losses.

Numerical solutions for $x(t)$ are obtained by integrating Equation 20 using the source $S(x, t)$ in Equation 21, together with the additional noise ΔS. Integrating over one event interval, $\Delta t_i = t_i - t_{i-1}$, gives

$$x(t_i) = x(t_{i-1}) \exp(-\Delta t_i / \tau_d) + g_i + q\, w_i \tag{28}$$

where w_i is a random variable drawn from a normal distribution N(0, Δt_i). Allowances for a finite-duration source event are handled by numerically integrating a bell-shaped time dependence in S instead of a $\delta(t)$ function. Equivalent results can be obtained by convolving the solution in Equation 28 with a bell-shaped filter function, identical to the finite-duration time dependence for S. We approximate this solution using a running average with a filter width equal to 50% of the overturn time (see Appendix B for details).

5.1. Parameters of the Stochastic Models

Predictions of the stochastic models are compared with the geodynamo models in two different ways. One option is to run long realizations of the process to recover trends from the time series. Each finite realization is unique but uncertainties in the statistics are reduced when the realizations are long. Alternatively, we can define a probability distribution for $x(t)$, which we denote by $p(x, t)$. Expected values for the trends can then be computed directly from $p(x, t)$. In either case we need to define the parameters in the stochastic model. Specifically, we need

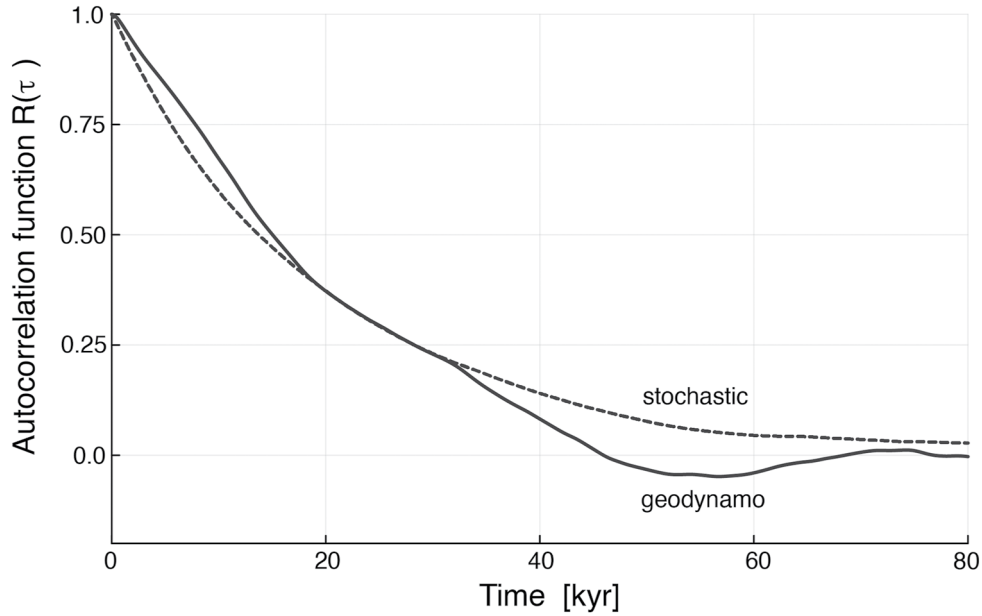

Figure 6. Autcorrelation functions for $x(t)$ from geodynamo model B3 (solid line) and from the corresponding stochastic model (dashed line). An effective dipole decay time of $\tau_d = 20$ kyr is computed from the geodynamo model and adopted in the stochastic model.

to specify the dipole decay time, τ_d, and the average recurrence time, θ, for the Poisson process. We also need to define the limits $[A_{\min}, A_{\max}]$ on the amplitude distribution $U(A)$.

The dipole decay time is computed from the autocorrelation function $R(\tau)$ for the dipole moment $x(t)$, based on time series from the geodynamo models (e.g., Buffett & Matsui, 2015). Integrating $R(\tau)$ over the lag time τ gives an estimate of the effective τ_d. Figure 6 shows $R(\tau)$ for Case B3, compared with the autocorrelation function from the stochastic model when we adopt the value $\tau_d = 20$ kyr. This value is slightly less than half the dipole decay time expected for the molecular diffusivity adopted in the geodynamo models ($\eta = 0.8$ m^2 s^{-1}). The difference is attributed to the effects of turbulent diffusion (Holdenried-Chernoff & Buffett, 2022). The upper and lower limits on A are set by matching the mean and standard deviation of $x(t)$ for Case B3. Finally, the average recurrence time θ is adjusted to produce the skewness required by the geodynamo models. Choosing a longer recurrence time gives a higher skewness (Realizations for Case B3 have $\theta = \lambda^{-1} = 0.1$ kyr and we remove the additional white noise ΔS by letting $q^2 = 0$). All five parameters in the stochastic model are iteratively adjusted to give reasonable agreement with the geodynamo model.

Once the parameters of the stochastic model are defined we are able to directly calculate the coefficients of the Kramers-Moyal expansion for the probability distribution $p(x, t)$. Explicit expressions for the coefficients have previously been derived for the stochastic model with δ-function convection events (Buffett et al., 2022). The relevant coefficients for present purposes include the diffusion coefficient, D_2,

$$D_2(x) = \frac{1}{2}\lambda\langle A^2\rangle x^2 f(x)^2 + \frac{1}{2}q^2 \tag{29}$$

and the skewness term, D_3,

$$D_3(x) = \frac{1}{6}\lambda\langle A^3\rangle x^3 f(x)^3 \tag{30}$$

where the moments of the amplitude A are defined by

$$\langle A^n\rangle = \int_{-\infty}^{\infty} A^n U(A)\, dA. \tag{31}$$

We use these coefficients to compute the expected values of the trends. Trends at small w are approximated as

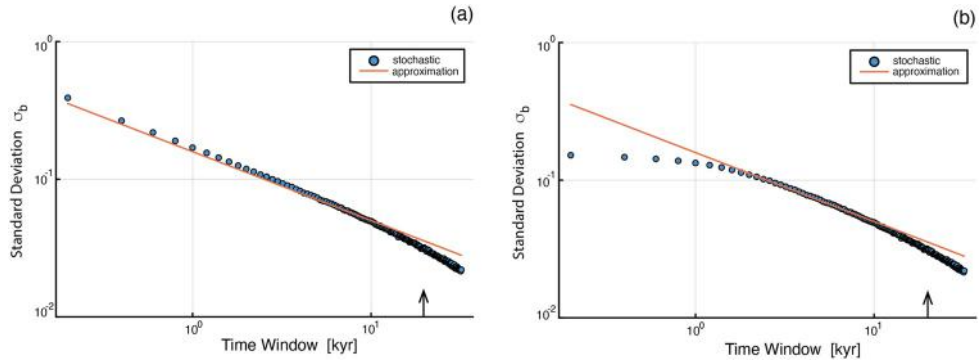

Figure 7. Predictions of σ_b for a stochastic model with δ-function convective events (a) and finite-duration convective events (b). Allowing for finite-duration convection events causes σ_b to deviate from the approximation (in red) at small w. Arrows indicate the effective dipole decay time τ_d for Case B3.

$$b = \frac{x(t+w) - x(t)}{w} \tag{32}$$

so the expected value of b^2 is

$$E\left(b^2\right) = \frac{\left\langle [x(t+w) - x(t)]^2 \right\rangle}{w^2} = \frac{2D_2(x)}{w} \tag{33}$$

where we have used the relationship (Risken, 1996)

$$\left\langle [x(t+w) - x(t)]^n \right\rangle = n! D_n(x) w \tag{34}$$

for small w. Equation 33 is equivalent to the expression for σ_b in Equation 13 because $E(b) = 0$ when the trends fluctuate zero. Similarly, we can define the third moment as

$$E\left(b^3\right) = \frac{6D_3(x)}{w^2} \tag{35}$$

so the skewness becomes

$$s = \frac{6D_3(x)}{(2D_2(x))^{3/2} w^{1/2}}. \tag{36}$$

Both $D_3(x)$ and $D_2(x)$ are evaluated at $x = < x >$ to be consistent with the requirement that $E(b) = 0$. In effect we set $x = \langle x \rangle$ to ensure that $D_1(x)$ and the mean trend both vanish. We now compare these approximations with realizations of the stochastic models.

5.2. Variance of Trends in Stochastic Model

Predictions for σ_b from a long realization of the stochastic model (Case B3) are shown in Figure 7. We consider both δ-function convection events in (a) and finite-duration convective events in (b). The former is equivalent to models with uncorrelated noise, whereas the latter is equivalent to models with correlated noise. The approximation shown in Figure 7 is taken from Equation 33, which is based on the assumption of uncorrelated noise. We find that the approximation agrees reasonably well with the δ-function convective events in (a) when the time window is less than the dipole decay time τ_d. A steeper decline in σ_b is expected for longer w (e.g., Nijsse et al., 2019) and we observed this behavior in the realization of the stochastic model. Qualitatively similar results were obtained in the geodynamo models (see Figure 2). By comparison, the predictions for the finite-duration convection events show weak variations in σ_b when w is less than 1 kyr. Both the shape and the overall magnitude of σ_b from the finite-duration stochastic model are broadly consistent with the geodynamo models. However, there are notable differences. For example, at long w the stochastic and geodynamo models appear to deviate from the approximate estimate at slightly different values of w. There are also small differences at short w where the

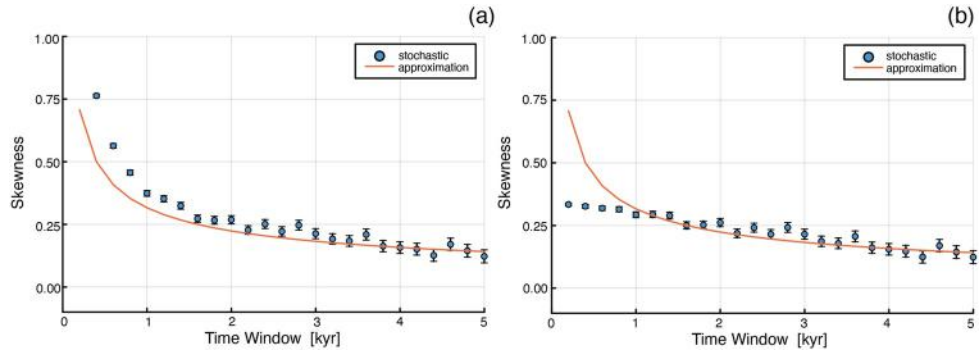

Figure 8. Predictions of s for Case B3 stochastic model with δ-function convective events (a) and finite-duration convective events (b). Allowing for finite-duration convection events in (b) suppresses large values of s at small w. Gradual decreases in s are observed at large w.

stochastic and geodynamo models depart from the approximate estimate due to the influence of correlated noise. Despite these differences the agreement is fairly good, especially given that no information about the dipole trend is used in the construction of the stochastic model.

5.3. Skewness of Trends in Stochastic Model

Predictions for s from the stochastic model are shown in Figure 8 for Case B3. Once again we distinguish between δ-function convection events in (a) and finite-duration convection events in (b). The stochastic model in (a) reproduces a sharp increase in s at small w, although there are differences in detail from the approximation (in red). Finite-duration convection events in (b) eliminate the sharp increase in s at small w. Instead, the estimates of s decrease slowly with the length of the time window. At larger w the stochastic model with correlated noise is consistent with the approximate estimate from Equation 36, suggesting that the duration of the convection events is not important for dynamics at long timescales. The magnitude of s and the general dependence on w is broadly consistent with the geodynamo model for Case B3.

Lower skewness for Cases TB0 and TB1 is achieved by lowering the recurrence time to $\theta = 0.03$ kyr. We also introduce a small additional noise by setting $q^2 = 0.04 \times 10^{44}$ A^2 m^4 kyr^{-1}. This additional noise is intended to represent the larger variability in the electric current in the top- and bottom-driven geodynamo models. In practical terms the introduction of additional noises causes symmetric fluctuations in the dipole trends at short w, which reduces the skewness. A decrease in the skewness at larger w is accomplished through the choice of a shorter recurrence time. This combination of changes to θ and q^2 are sufficient to bring the skewness for TB0 and TB1 down to $s = 0.04$ at small w. This value is within the uncertainties of the average skewness from the top- and bottom-driven geodynamo models.

6. Discussion and Conclusions

Stochastic models are capable of reproducing many features of the dipole trends from the geodynamo models. We can account for the variance of trends by simply requiring the stochastic model to reproduce the mean and variance of $x(t)$ from the geodynamo model. An additional constraint on the dipole decay time comes from the correlation time for $x(t)$ in the geodynamo models. We can also quantitatively account for the skewness of dipole trends by adjusting the recurrence time of convective events and the background level of noise associated with ΔS. While there are small departures from the results of the geodynamo models, the stochastic models capture the overall magnitude of σ_b and s. They also characterize the general dependence of σ_b and s on the time window w.

Significant levels of skewness from the geodynamo models confirm that asymmetries in dipole growth and decay are physically plausible. While very little skewness is produced when convection is driven by buoyancy at the top and bottom boundaries, we obtained skewed trends for all bottom-driven models. The latter style of convection is thought to be representative of conditions in the present-day Earth. Introducing a layer of stratified fluid at the top of the core increases the level of skewness in the geodynamo models to values in excess of $s = 0.5$. On the other hand, the geodynamo models produce much lower skewness at time windows approaching tens of kyr. These

are the relevant time windows for observations of skewness in the paleomagnetic record (Avery et al., 2017). Low levels of skewness in the paleomagnetic record for short windows ($w < 10$ kyr) have been attributed to the influence of measurement error (Buffett et al., 2022). Such low values at short w are not observed (or expected) in the geodynamo models.

We now turn to the question of what the stochastic model tells us about the paleomagnetic field. Skewness of dipole trends from PADM2M is nominally $s \approx 0.5$ for time windows around $w = 20$ kyr (Buffett et al., 2022). Similar conclusions were drawn by Avery et al. (2017), based on the statistics of the time derivative of PADM2M after filtering the record to remove periods shorter than 20–30 kyr. Long recurrence times, possibly in excess of 3 kyr, are needed to account for the observed skewness. What does this tell us about the nature of convection in the core? Recurrence times in the bottom-driven geodynamos are roughly 7% of the overturn time, which is shorter than the duration of the convection events (nominally 50% of the overturn time). We can put these quantities into absolute terms by adopting the nominal overturn time of 1.4 kyr from the geodynamo models. The recurrence time means that plumes are leaving the inner-core boundary every 100 years or so. These plumes are expected to survive for about 700 years as they rises through the core.

A recurrence time of 3 kyr from the paleomagnetic record raises an interesting question. How can the recurrence time of convective events be much longer than the 140-year overturn time in the Earth's core (e.g., Aubert & Gillet, 2021)? One interpretation is that a small fraction of the cyclonic events contribute substantially to dipole generation. Plumes may rise from the inner-core boundary on decade timescales (based on an overturn time of 140 years). These plumes are expected to travel upwards for 60–70 years before they are disrupted. During this time the buoyant plumes lift and twist the magnetic field to produce loops. A bottleneck in generating the dipole field may involve the steps of separating the upward and downward limbs of magnetic loops and expelling one of these limbs from the core. From this perspective the recurrence time might refer to flux expulsion events rather than the timing of individual plumes in the core. Less than 1% of these convective plumes are expected to cause flux expulsion if we want to lower the recurrence time from decades to thousands of years. Stratification at the top of the core may help to reduce the frequency of large expulsion events. While none of these arguments rule out the possibility of other physical processes regenerating magnetic field on shorter timescales (e.g., Davidson, 2014), it appears that large and infrequent flux expulsion events are required to account for the skewness of trends in the paleomagnetic record.

A related question is why we do not see long recurrence times in the geodynamo models. One source of difference in the geodynamo models is related to the value of Pm. All geodynamo models have Pm close to one, whereas the value of Pm in the core is nominally 10^{-6}. Such low values of Pm are expected to cause a separation of scales between the magnetic and velocities fields (e.g., Schaeffer et al., 2017). Low viscosity enables small-scale flow to persist, whereas higher values of magnetic diffusivity confine the magnetic field to relatively large scales. Small-scale flow should be characterized by low (local) values of Rm, which could potentially promote flux expulsion. On the other hand, the large-scale value of Rm in the Earth's core (nominally 500 to 1,000) is higher than the values in the geodynamo models (i.e., 130 to 160). The balance of these two factors is difficult to assess with the numerical results in hand. Our numerical models do not reveal a significant dependence on Pm when the value of Rm is held (nearly) fixed. However, the range of parameter values explored in this study is tiny compared to the values expected in the core. More realistic models might shed light on this question if the simulations could be run long enough to collect reliable statistics for the dipole trend.

Appendix A: Short-Time Description of Flux Expulsion

A quantitative assessment of flux expulsion in this study is based on prior numerical studies in a 2D Cartesian geometry (Bloxham, 1986; Troyano et al., 2020). Below we use x to denote the horizontal position and z to indicate the depth below the CMB. The model setup for Bloxham (1986) and configuration 3 of Troyano et al. (2020) involves a pair of counter-rotating eddies of size l in a conducting fluid with a constant initial horizontal field $B_x(0)$. Upwelling at the center of domain with amplitude u compresses the initial field toward the insulating region above the fluid, allowing a vertical component of magnetic field, $B_z(t)$, to diffuse into the insulating layer. A perfectly conducting boundary condition on the lower boundary fixes the initial magnetic field at the base of the calculation.

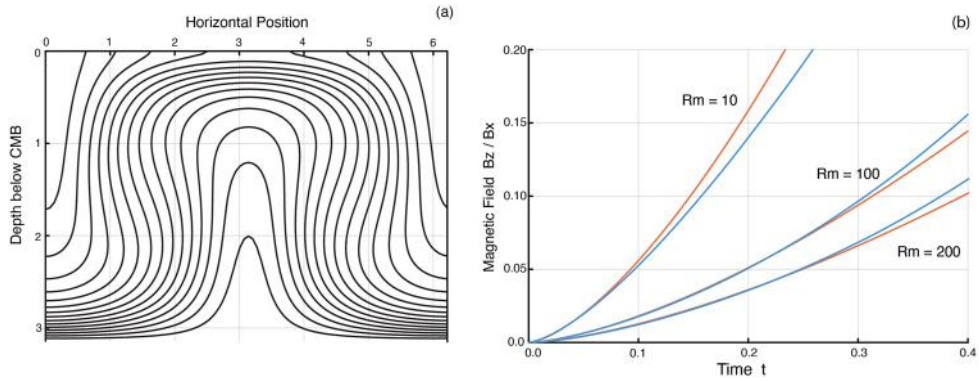

Figure A1. Numerical solution for magnetic-flux expulsion below the CMB. (a) Lines of constant magnetic potential **A** reveal the distortion of a horizontal magnetic field by upwelling and downwelling fluid motion. Magnetic field diffuses into the insulating region ($z < 0$) over time t. By comparison, no flux expulsion occurs at $z = \pi$ in the presence of perfectly conducting boundary conditions. (b) Short-time solutions for $B_z(t)/B_x(0)$ are computed for several values of *Rm*. The numerical solutions (in blue) are compared with an approximate solution from Equation 19 (in red).

Bloxham (1986) gives a detailed description of the numerical method. A very similar approach is followed by Troyano et al. (2020) to show that steady solutions emerge after 5 to 10 advection times (defined as l/u). The duration of upwelling in the geodynamo models is shorter than the time required to reach steady state, so we focus on a simple scaling relationship to characterize the behavior at short times. Our implementation of the model in Bloxham (1986) is used to validate this approximation (see Figure A1).

Flux expulsion can be represented as a superposition of two processes. Vertical flow u_z distorts the initial magnetic field $B_x(0)$ to produce a vertical component $B_z(t)$ inside the fluid. Diffusion allows this vertical component to escape into the insulating region. At large *Rm* and short times we expect

$$\frac{\partial B_z}{\partial t} = B_x(0)\frac{\partial u_z}{\partial x} \approx B_x(0)\frac{u}{l} \tag{A1}$$

so the ratio $B_z(t)/B_x(0)$ inside the fluid increases linearly with time. This field remains trapped inside the fluid in the absence of magnetic diffusion. Enabling diffusion allows a narrow region at the top of the core to expel lines of magnetic field. The depth of this region at short times should be set by the magnetic diffusion distance $l_\eta = \sqrt{\eta t}$. Because the number of field lines expelled from the core increases with l_η, we propose that the expelled fraction is proportional to

$$\frac{B_z^{ex}(t)}{B_x(0)} \sim \frac{B_z(t)}{B_x(0)}\left(\frac{l_\eta}{l}\right). \tag{A2}$$

Combining Equations A1 and A2 gives

$$\frac{B_z^{ex}(t)}{B_x(0)} \sim \frac{u\,\eta^{1/2}t^{3/2}}{l^2}, \tag{A3}$$

which reduces to Equation 19 after expressing t in nondimensional form using the advection time l/u. A single constant of proportionality is sufficient to account for all of the numerical results at short times.

Appendix B: Finite-Duration Convection Events

Generation of the dipole moment in the stochastic model is due to a series of cyclonic convection events. In the vicinity of a single event at $t = 0$ the dipole moment evolves according to

$$\frac{dx}{dt} = g(x)\delta(t) - \frac{x}{\tau_d} \tag{B1}$$

where $g(x)$ is the amplitude of the event. Solutions for $x(t)$ on either side of the event (i.e., $t \neq 0$) describe the decay of the dipole moment at a rate specified by the decay time τ_d. During the convective event at $t = 0$, the solution for $x(t)$ jumps by an amplitude $g(x\_)$ from its initial value at $x = x\_$. This definition is in accordance with the usual Itô interpretation (e.g., Oksendal, 2003).

Finite-duration convection events are introduced by replacing $\delta(t)$ with a symmetric function $f(t)$, which satisfies the condition

$$\int_{-\infty}^{\infty} f(t)\,dt = 1 \tag{B2}$$

and has a finite duration defined by the second moment

$$\Delta^2 = \int_{-\infty}^{\infty} t^2 f(t)\,dt. \tag{B3}$$

Evolution of the dipole moment for finite-duration events now obeys

$$\frac{dx}{dt} = g(x\_)f(t) - \frac{x}{\tau_d}, \tag{B4}$$

where the event amplitude has been fixed at the value from Equation B1. This assumption is reasonable when the changes in $x(t)$ are small over the timescale Δ. Integrating Equation B4 for $x(t)$ using an initial condition $x(t_0)$ at $t = t_0$ gives

$$x(t) = x(t_0)e^{-(t-t_0)/\tau_d} + \int_{t_0}^{t} f\left(t'\right)e^{-(t-t')/\tau_d}\,dt'. \tag{B5}$$

A representative solution using a Gaussian function for $f(t)$ is shown in Figure B1a. For comparison, we also plot a solution for $x(t)$ from Equation B1. Because the initial condition and amplitude of the convection event are the same, the values for $x(t)$ converge at $t = 1$ kyr. The only difference between the solutions in Figure B1a is the duration of the increase in $x(t)$ over the convective event.

We can interpret the solution in Equation B5 as a convolution of the forcing $f(t)$ with the Green's function for the impulse response. Alternatively, a suitable change of variables allows us to write the solution as a convolution of a filter function $f(t)$ with the solution from Equation B1. This means we can recover the finite-duration solution by smoothing the uncorrelated solution with a suitably chosen filter function $f(t)$. Ideally, we would want to use a filter function that coincides with the temporal dependence of the finite-duration events. However, we can still obtain reasonable solutions using a different filter function, as long as the width of the filter is the same. Figure B1b compares the solution from Equation B5 with a filtered version of the solution to Equation B1, where we use a box-car function for $f(t)$. We can expect reasonable agreement in the trends from these two solutions

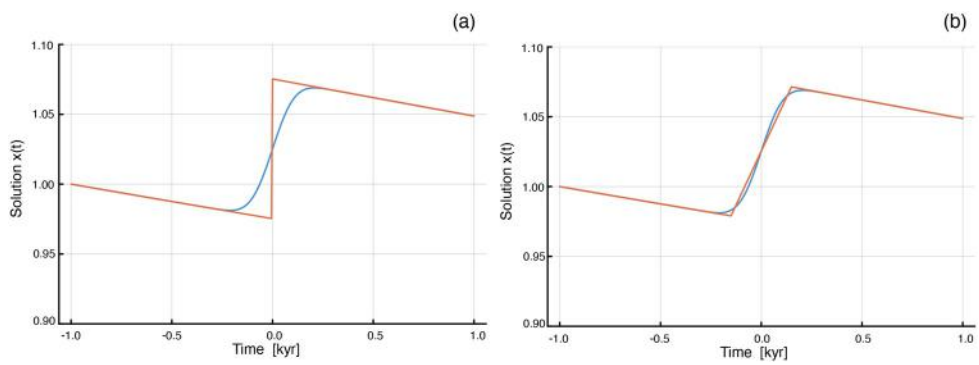

Figure B1. Evolution of $x(t)$ in the stochastic model across a single convective event. (a) Comparison of δ-function (red) and finite-duration (blue) convective event. (b) Temporal filtering of δ-function solution with a box-car function (red) approximates the finite-duration convective event.

when the window w is long compared with Δ. In this study we use a box-car filter with a width equal to 50% of the overturn time to define the stochastic model with finite-duration convection events.

Data Availability Statement

The dynamo model *Calypso* (version 1.2.0) is developed and distributed by the Computational Infrastructure for Geodynamics with support from the US National Science Foundation (EAR-1550901). The code can be obtained from Zenodo (Matsui et al., 2017). Numerical solutions used in this study are available in the Dryad Digital Repository (Davis & Buffett, 2021). The paleomagnetic model PADM2M was obtained from the EarthRef Digital Archive (Zeigler, 2011) and the stochastic model is available from Zenodo (Buffett, 2021).

Acknowledgments
I thank Daria Holdenried-Chernoff for discussion and comments on the original manuscript. Detailed and constructive reviews by Phil Livermore and Julien Aubert substantially improved the paper. The initial phase of this work was supported by the National Science Foundation (Grant EAR-1644644).

References

Aubert, J., & Gillet, N. (2021). The interplay of fast waves and slow convection in geodynamo simulations nearing Earth's core conditions. *Geophysical Journal International*, *225*(3), 1854–1873. https://doi.org/10.1093/gji/ggab054

Aurnou, J. M., & King, E. M. (2017). The cross-over to magnetostrophic convection in planetary dynamo systems. *Proceedings of the Royal Society A: Mathematical, Physical and Engineering Sciences*, *473*(2199), 20160731. https://doi.org/10.1098/rspa.2016.0731

Avery, M. S., Constable, C. G., Davies, C. J., & Gubbins, D. (2019). Spectral methods for analyzing energy balances in geodynamo simulations. *Physics of the Earth and Planetary Interiors*, *286*, 127–137. https://doi.org/10.1016/j.pepi.2018.10.002

Avery, M. S., Gee, J. S., & Constable, C. C. (2017). Asymmetry in growth and decay of the geomagnetic dipole revealed in seafloor magnetization. *Earth and Planetary Science Letters*, *467*, 78–88. https://doi.org/10.1016/j.epsl.2017.03.020

Bloxham, J. (1986). The expulsion of magnetic flux from the earth's core. *Geophysical Journal of the Royal Astronomical Society*, *87*(2), 669–678. https://doi.org/10.1111/j.1365-246x.1986.tb06643.x

Buffett, B. (2021). Stochastic 1D: v1.0.0 [Software]. Zendo. https://doi.org/10.5281/zenodo.5557901

Buffett, B., Avery, M. S., & Davis, W. (2022). A physical interpretation of asymmetric growth and decay of the geomagnetic dipole moment. *Geochemistry, Geophysics, Geosystems*, *23*(3), e2021GC010239. https://doi.org/10.1029/2021GC010239

Buffett, B., Davis, W., & Avery, M. S. (2019). Variability of millennial-scale trends in the geomagnetic axial dipole. *Geophysical Research Letters*, *46*(24), 14450–14458. https://doi.org/10.1029/2019GL085909

Buffett, B., Knezek, N., & Holme, R. (2016). Evidence for MAC waves at the top of Earth's core and implications for variations in the length of day. *Geophysical Journal International*, *204*(3), 1789–1800. https://doi.org/10.1093/gji/ggv552

Buffett, B., & Matsui, H. (2015). A power spectrum for the geomagnetic dipole moment. *Earth and Planetary Science Letters*, *411*, 20–26. https://doi.org/10.1016/j.epsl.2014.11.045

Cattaneo, F., & Tobias, S. M. (2014). On large-scale dynamo action at high magnetic Reynolds number. *The Astrophysical Journal*, *789*, 1–10. https://doi.org/10.1088/0004-637X/789/1/70

Chandrasekhar, S. (1981). *Hydrodynamic and hydromagnetic stability*. Dover.

Constable, C., Korte, M., & Panovska, S. (2016). Persistent high paleosecular variations in the southern hemisphere for at least 10000 years. *Earth and Planetary Science Letters*, *453*, 78–86. https://doi.org/10.1016/j.epsl.2016.08.015

Davidson, P. A. (2001). *An introduction to magnetohydrodynamics*. Cambridge University Press.

Davidson, P. A. (2014). The dynamics and scaling laws of planetary dynamos driven by inertial waves. *Geophysical Journal International*, *198*(3), 1832–1847. https://doi.org/10.1093/gji/ggu220

Davis, W., & Buffett, B. (2021). Inferring core processes using stochastic models of the geodynamo [Dataset]. Dryad, *228*, 1478–1493. https://doi.org/10.6078/D1WB0S

Davis, W., & Buffett, B. (2022). Inferring core processes using stochastic models of the geodynamo. *Geophysical Journal International*, *228*(3), 1478–1493. https://doi.org/10.1093/gji/ggab412

Gomi, H., & Hirose, K. (2015). Electrical resistivity and thermal conductivity of hcp fe-ni alloys under high pressure: Implications for thermal convection in Earth's core. *Physics of the Earth and Planetary Interiors*, *247*, 2–10. https://doi.org/10.1016/j.pepi.2015.04.003

Holdenried-Chernoff, D., & Buffett, B. A. (2022). Evidence for turbulent magnetic diffusion in Earth's core. *Geochemistry, Geophysics, Geosystems*, *23*(12), e2022GC010672. https://doi.org/10.1029/2022GC010672

Jackson, J. P. (1999). *Classical electrodynamics*. Wiley.

Joanes, D. N., & Gill, C. A. (1989). Comparing measures of sample skewness and kurtosis. *Journal of the Royal Statistical Society: Series D*, *47*(1), 183–189. https://doi.org/10.1111/1467-9884.00122

Kageyama, A., & Sato, T. (1997). Generation mechanism of a dipole field by a hydromagnetic dynamo. *Physics Reviews*, *55*(4), 4617–4626. https://doi.org/10.1103/PhysRevE.55.4617

Kutzner, C., & Christensen, U. R. (2002). From stable dipolar towards reversing numerical dynamos. *Physics of the Earth and Planetary Interiors*, *131*(1), 29–45. https://doi.org/10.1016/S0031-9201(02)00016-X

Levy, E. H. (1972). Kinematic reversal schemes for the geomagnetic dipole. *The Astrophysical Journal*, *171*, 635–642. https://doi.org/10.1086/151318

Livermore, P. W., Finlay, C. C., & Bayliff, M. (2020). Recent north magnetic pole acceleration towards Siberia caused by flux lobe elongation. *Nature Geoscience*, *13*(5), 387–391. https://doi.org/10.1038/s41561-020-0570-9

Matsui, H., Heien, E., Lokavarapu, H., & Esser, T. (2017). Calypso v1.2.0 computational infrastructure for geodynamics [Software]. Zenodo. https://doi.org/10.5281/zenodo.890016

Matsui, H., King, E., & Buffett, B. (2014). Multiscale convection in a geodynamo simulation with uniform heat flux along the outer boundary. *Geochemistry, Geophysics, Geosystems*, *15*(8), 3212–3225. https://doi.org/10.1029/2014GC005432

Moffatt, H.-K. (1978). *Magnetic field generation in electrically conducting fluids*. Cambridge University Press.

Nijsse, F., Cox, P., Huntingford, C., & Williamson, M. (2019). Decadal global temperature variability increases strongly with climate sensitivity. *Nature Climate Change*, *9*(8), 598–601. https://doi.org/10.1038/s41559-019-0527-4

Oksendal, B. (2003). *Stochastic differential equations: An introduction with applications*. Springer.

Olson, P., & Amit, H. (2006). Changes in Earth's dipole. *Naturwissenschaften*, *93*(11), 519–542. https://doi.org/10.1007/s00114-006-0138-6

Panovska, S., Constable, C., & Korte, M. (2018). Extending global continuous geomagnetic field reconstructions on timescales beyond human civilization. *Geochemistry, Geophysics, Geosystems*, *19*(12), 4757–4772. https://doi.org/10.1029/2018GC007966

Parker, E. N. (1955). Hydromagnetic dynamo models. *The Astrophysical Journal*, *122*, 293–314. https://doi.org/10.1086/146087

Risken, H. (1996). *The Fokker-Planck equation*. Springer.

Schaeffer, N., Jault, D., Nataf, H. C., & Fournier, A. (2017). Turbulent geodynamo simulations: A leap towards Earth's core. *Geophysical Journal International*, *211*, 1–29. https://doi.org/10.1093/gji/ggx265

Scullard, C. R., & Buffett, B. A. (2018). Probabilistic structure of the geodynamo. *Physical Review E - Statistical Physics, Plasmas, Fluids, and Related Interdisciplinary Topics*, *98*(6), 063112. https://doi.org/10.1103/PhyRevE.98.063112

Tennekes, H., & Lumley, J. L. (1983). *A first course in turbulence*. MIT Press.

Tobias, S. M. (2021). The turbulent dynamo. *Journal of Fluid Mechanics*, *912*, P1. https://doi.org/10.1017/jfm.2020.1055

Troyano, M., Fournier, A., Gallet, Y., & Finlay, C. C. (2020). Imprint of magnetic flux expulsion at the core-mantle boundary on geomagnetic field intensity variations. *Geophysical Journal International*, *221*(3), 1984–2009. https://doi.org/10.1093/gji/ggaa126

Valet, J. P., Meynadier, L., & Guyodo, Y. (2005). Geomagnetic dipole strength and reversal rate over the past two million years. *Nature*, *435*(7043), 802–805. https://doi.org/10.1038/nature03674

Zeigler, L. B. (2011). Paleomagnetic axial dipole field model for 0-2 Ma [Dataset]. ERDA. https://earthref.org/ERDA/1138

Ziegler, L., & Constable, C. (2011). Asymmetry in growth and decay of the geomagnetic dipole. *Earth and Planetary Science Letters*, *312*(3–4), 300–304. https://doi.org/10.1016/j.epsl.2011.10.019

Ziegler, L., Constable, C. G., Johnson, C. L., & Tauxe, L. (2011). PADM2M: A penalized maximum likelihood model of the 0-2 Ma paleomagnetic axial dipole moment. *Geophysical Journal International*, *184*(3), 1069–1089. https://doi.org/10.1111/j.1365-246X.2010.04905.x